

# Chemical Science

Accepted Manuscript

This article can be cited before page numbers have been issued, to do this please use: M. Mu, J. Chen, X. Xue, Y. Yang, R. Qi, Y. Wang, D. Liu, L. Shang, W. Jiang, X. Shao, Z. Chen, B. Zhao and W. Song, *Chem. Sci.*, 2025, DOI: 10.1039/D5SC04633E.



This is an Accepted Manuscript, which has been through the Royal Society of Chemistry peer review process and has been accepted for publication.

Accepted Manuscripts are published online shortly after acceptance, before technical editing, formatting and proof reading. Using this free service, authors can make their results available to the community, in citable form, before we publish the edited article. We will replace this Accepted Manuscript with the edited and formatted Advance Article as soon as it is available.

You can find more information about Accepted Manuscripts in the [Information for Authors](#).

Please note that technical editing may introduce minor changes to the text and/or graphics, which may alter content. The journal's standard [Terms & Conditions](#) and the [Ethical guidelines](#) still apply. In no event shall the Royal Society of Chemistry be held responsible for any errors or omissions in this Accepted Manuscript or any consequences arising from the use of any information it contains.

## ARTICLE

Insight of Interfacial Water & Key Intermediates at Cu<sub>95</sub>Co<sub>5</sub> Aerogels for Electrocatalytic Nitrate-to-Ammonia ConversionMing Mu<sup>a</sup>, Junjie Chen<sup>a,b</sup>, Xiangxin Xue<sup>c</sup>, Yumei Yang<sup>a</sup>, Ruikai Qi<sup>d</sup>, Yuezhu Wang<sup>d</sup>, Di Liu<sup>a</sup>, Lijia Shang<sup>a</sup>, Wenji Jiang<sup>a</sup>, Xinyi Shao<sup>a</sup>, Zheng-jie Chen<sup>e\*</sup>, Bing Zhao<sup>a</sup>, Wei Song<sup>a\*</sup>Received 00th January 20xx,  
Accepted 00th January 20xx

DOI: 10.1039/x0xx00000x

Electrocatalytic nitrate reduction (NO<sub>3</sub>RR) to ammonia presents a sustainable route for pollutant remediation and green synthesis, yet challenges persist in achieving high efficiency and selectivity. Herein, we report a cobalt-doped copper aerogel (Cu<sub>95</sub>Co<sub>5</sub>) synthesized via one-step co-reduction, demonstrating exceptional NO<sub>3</sub>RR performance with 94.91% faradaic efficiency at −0.6 V and 31.15 mg mg<sub>cat</sub><sup>−1</sup> cm<sup>−2</sup> h<sup>−1</sup> NH<sub>3</sub> yield at −0.7 V vs. RHE. The system achieves an impressive energy efficiency of 31.03% and enables a record-low ammonia production cost of \$0.53 kg<sup>−1</sup>. Multiscale characterization reveals that Co doping induces lattice contraction, optimizes d-band positioning, and enhances interfacial K<sup>+</sup>·H<sub>2</sub>O interactions, collectively promoting water dissociation and \*H generation. The combination of operando spectroscopies (SERS, ATR-FTIR, DEMS) and density functional theory (DFT) calculations elucidate a stepwise hydrogenation pathway: \*NO<sub>3</sub> → \*NO<sub>2</sub> → \*NO → \*NH<sub>2</sub>OH → \*NH<sub>3</sub>, with the rate-determining step (RDS) identified as \*NO hydrogenation to \*NHO. The hierarchical porosity of the aerogel facilitates mass transport while Cu-Co synergy suppresses hydrogen evolution reactions via electronic modulation. Practical viability is demonstrated through stable 12-hour operation in a Zn-NO<sub>3</sub><sup>−</sup> battery. This work provides insights into Cu-Co catalysis and establishes design principles for high-performance NO<sub>3</sub>RR systems.

## Introduction

The pervasive issue of nitrate (NO<sub>3</sub><sup>−</sup>) pollution poses a significant threat to aquatic ecosystems and human health, with excessive accumulation in water bodies driving eutrophication and contributing to diseases such as methemoglobinemia and gastric cancer<sup>1</sup>. Annual discharges of nitrate from industrial and agricultural sources exceed millions of tons, while conventional remediation techniques like ion exchange and reverse osmosis suffer from high energy costs and secondary contamination<sup>1</sup>. In recent years, the electrocatalytic nitrate reduction reaction (NO<sub>3</sub>RR) has emerged as a transformative strategy, combining pollutant remediation with resource recovery by converting NO<sub>3</sub><sup>−</sup> into high-value ammonia (NH<sub>3</sub>) through an eight-electron/nine-proton transfer pathway. This process not only enables sustainable NH<sub>3</sub> synthesis but also facilitates energy storage through integration with Zn-NO<sub>3</sub><sup>−</sup> batteries systems<sup>2</sup>. Compared to the Haber-Bosch process—a century-old

industrial method consuming 2% of global energy and emitting 1% of CO<sub>2</sub> annually<sup>3</sup>—NO<sub>3</sub>RR leverages the low dissociation energy of N=O bonds (204 kJ mol<sup>−1</sup>) and high solubility of NO<sub>3</sub><sup>−</sup> (10.4 mol L<sup>−1</sup>) in water, offering a greener alternative with reduced energy barriers and enhanced economic viability<sup>4</sup>.

Despite the superior NH<sub>3</sub> synthesis activity of noble metals (e.g., Ru, Rh, Pd, Au), their scarcity and high cost drive exploration of earth-abundant transition metal electrocatalysts<sup>5</sup>. Notably, transition-metal alloys, transition-metal oxides, and organometallic compounds (such as transition-metal phthalocyanines and metal-organic frameworks) often exhibit excellent catalytic performance<sup>6–11</sup>. Copper-based catalysts have garnered attention for NO<sub>3</sub>RR due to their unique 3d<sup>10</sup>4s<sup>1</sup> electronic configuration. The fully occupied 3d orbitals align energetically with the π\* antibonding orbitals of NO<sub>3</sub><sup>−</sup>, facilitating electron transfer, while their inherent low hydrogen adsorption energy suppresses competing hydrogen evolution reactions (HER), thereby enhancing NH<sub>3</sub> selectivity<sup>12–13</sup>. However, monometallic Cu catalysts face challenges such as insufficient active site exposure, limited proton hydrogen supply capacity and sluggish intermediate desorption kinetics. Recent efforts to optimize performance via stabilizing metastable amorphous structures<sup>14</sup>, oxygen vacancy modulation<sup>15</sup>, and heterostructure construction<sup>16–18</sup> are hindered by complex synthesis protocols, limiting scalability. The introduction of cobalt into Cu-based systems presents a promising solution<sup>19</sup>. Co can also modulate the surface electronic structure of the catalyst by altering the position of the d-band center, optimizes intermediate adsorption strength, complementing NO<sub>3</sub><sup>−</sup> activation and

<sup>a</sup> State Key Laboratory of Supramolecular Structure and Materials, College of Chemistry, Jilin University, Changchun 130012, PR China.

<sup>b</sup> State Grid Sichuan Electric Power Research Institute, Chengdu, 610041, China.

<sup>c</sup> Ministry of Education Key Laboratory of Preparation and Applications of Environmental Friendly Materials, Jilin Normal University, Changchun, 130103, P. R. China

<sup>d</sup> Alan G. MacDiarmid Institute, College of Chemistry, Jilin University, 2699 Qianjin Street, Changchun 130012, PR China.

<sup>e</sup> Faculty of Materials Science and Energy Engineering, Shenzhen University of Advanced Technology, Shenzhen, 518107, China

† Corresponding author: Wei Song E-mail address: weisong@jlu.edu.cn (W. Song).

Supplementary Information available: [details of any supplementary information available should be included here]. See DOI: 10.1039/x0xx00000x



deoxygenation capabilities of  $\text{Cu}^{20}$ . Synergistic Cu-Co systems exhibit enhanced catalytic efficiency through electronic and

investigating its  $\text{NO}_3\text{RR}$  performance and mechanism. The material integrates the hierarchical porosity of aerogels—

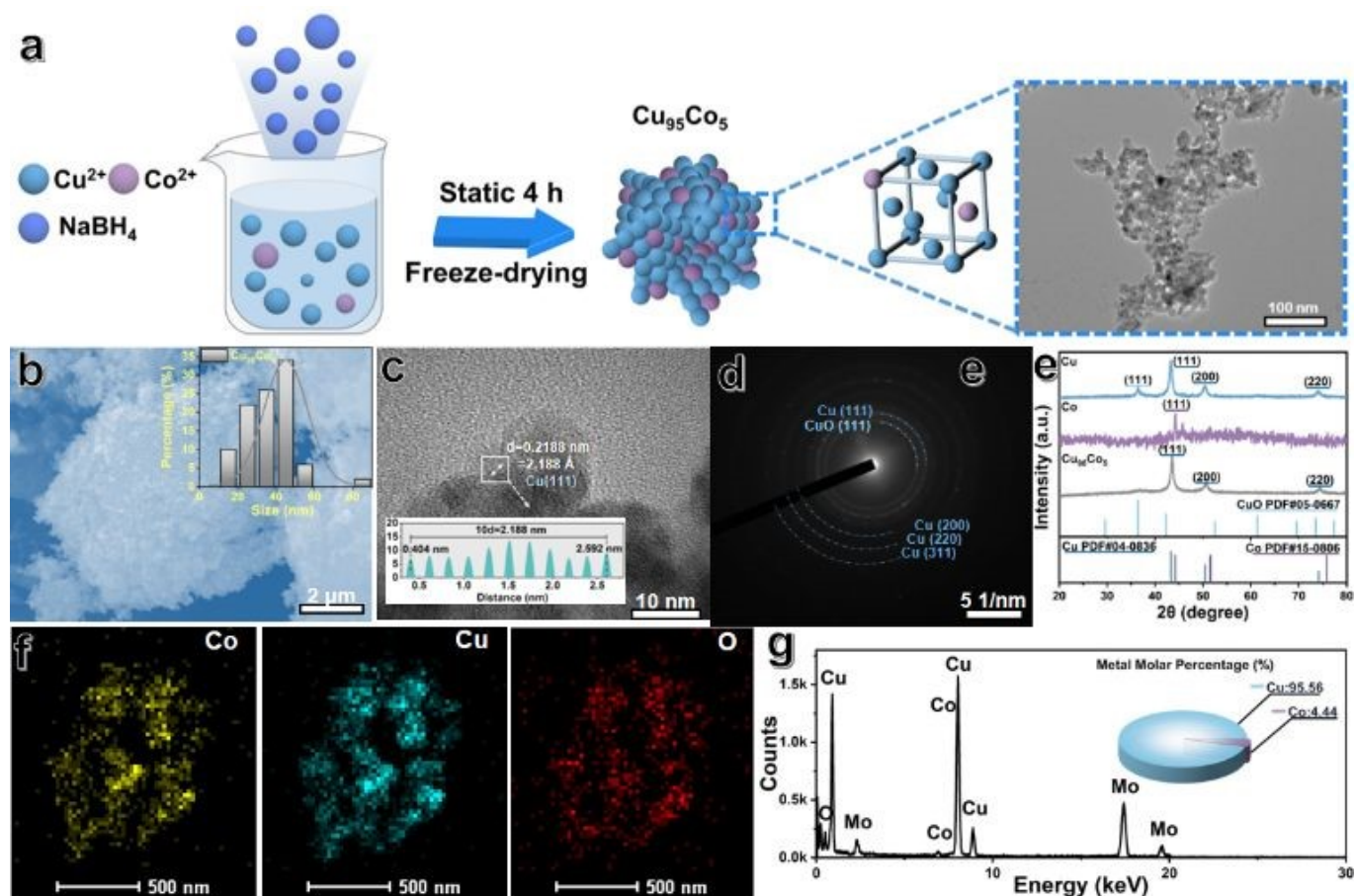


**Fig. 1** Characterization of  $\text{Cu}_{95}\text{Co}_5$  aerogel. (a) Schematic illustration of synthesis route of  $\text{Cu}_{95}\text{Co}_5$  aerogel. (b) TEM image of  $\text{Cu}_{95}\text{Co}_5$  aerogel. (c) HRTEM image of  $\text{Cu}_{95}\text{Co}_5$  aerogel. (d) Selected area electron diffraction (SAED) pattern of  $\text{Cu}_{95}\text{Co}_5$  aerogel. (e) XRD patterns of Cu aerogel, Co aerogel and  $\text{Cu}_{95}\text{Co}_5$  aerogel. (f) EDS mapping of  $\text{Cu}_{95}\text{Co}_5$  aerogel, showing the spatial distribution of Co (yellow), Cu (green) and O (red). (g) Pie chart of metal molar percentage of  $\text{Cu}_{95}\text{Co}_5$  aerogel measured by ICP. (h) XPS valence band spectra of Cu, Co, and  $\text{Cu}_{95}\text{Co}_5$  aerogel and its d-band center.

geometric effects. For instance, He et al. developed a Cu-Co sulfide-derived core-shell catalyst achieving 93.3%  $\text{NH}_3$  Faradaic efficiency (FE) in alkaline media, where the  $\text{Cu}/\text{CuO}_x$  core promotes  $\text{NO}_3^- \rightarrow \text{NO}_2^-$  conversion, and the  $\text{Co}/\text{CoO}$  shell accelerates  $\text{NO}_2^- \rightarrow \text{NH}_3$  hydrogenation<sup>21</sup>.

$\text{NO}_3\text{RR}$  involves multistep electron transfers and transient intermediates, challenging conventional ex situ characterization. In situ and quasi in situ spectroscopic techniques, including Fourier-transform infrared spectroscopy (FTIR), surface-enhanced Raman spectroscopy (SERS), electron paramagnetic resonance (EPR), and differential electrochemical mass spectrometry (DEMS) offer unprecedented capabilities to probe dynamic interfacial phenomena resolve molecular vibrations, unpaired electron states, and volatile intermediates at electrified interfaces, unveiling active sites and reaction pathways<sup>22-24</sup>. These atomic-scale insights guide rational design of high-activity/durability catalysts for sustainable ammonia synthesis.

In this work, we synthesize a cobalt-doped copper aerogel ( $\text{Cu}_{95}\text{Co}_5$ ) via a one-step co-reduction method, systematically

enhancing mass transport and active site accessibility—with Cu-Co electronic synergy, optimizes the d-band center.  $\text{Cu}_{95}\text{Co}_5$  achieves exceptional performance, delivering 94.91% FE and a  $\text{NH}_3$  yield of  $31.15 \text{ mg mg}_{\text{cat}}^{-1} \text{ cm}^{-2} \text{ h}^{-1}$  at  $-0.7 \text{ V}$  vs. RHE in  $1 \text{ M KOH}$ . In situ surface-enhanced Raman spectroscopy (SERS) reveals elevated interfacial  $\text{K}^+\cdot\text{H}_2\text{O}$  concentrations that accelerate water dissociation and  $\text{*H}$  generation. The combination of operando spectroscopy (SERS, ATR-FTIR, DEMS) and density functional theory (DFT) calculations elucidate a stepwise hydrogenation pathway:  $\text{*NO}_3 \rightarrow \text{*NO}_2 \rightarrow \text{*NO} \rightarrow \text{*NH}_2\text{OH} \rightarrow \text{*NH}_3$ , with the rate-determining step (RDS) identified as  $\text{*NO}$  hydrogenation to  $\text{*NHO}$ . Furthermore,  $\text{Cu}_{95}\text{Co}_5$  demonstrates  $>12 \text{ h}$  stable power output in a  $\text{Zn}-\text{NO}_3^-$  battery, underscoring its practical viability. This study elucidates the electronic structure modulation and interfacial kinetics governing Cu-Co synergy, providing a framework for designing high-performance  $\text{NO}_3\text{RR}$  catalysts. These insights advance the rational development of electrocatalytic ammonia synthesis technologies toward industrial scalability.





## Results and discussion

### Morphological and Structural Characterization

The 5% Co-doped Cu aerogel ( $\text{Cu}_{95}\text{Co}_5$  aerogel) was synthesized using via a co-reduction method, as illustrated in Fig. 1a. Specifically,  $\text{CuCl}_2$  and  $\text{CoCl}_2$  aqueous solutions were used, followed by dropwise addition of  $\text{NaBH}_4$  solution. After 4 hours of static aging at room temperature, the resulting product underwent thorough washing and freeze-drying processes. As revealed by scanning electron microscopy (SEM) in Fig. 1b, the obtained  $\text{Cu}_{95}\text{Co}_5$  aerogel exhibits a three-dimensional porous architecture comprising interconnected nanoparticles. The interconnected nanoporous networks facilitate rapid mass adsorption and transport. Comparative analysis with pure Cu and Co aerogels (Figs. S1-2) demonstrates that Co doping significantly modifies the morphological features, yielding a reduced average particle diameter of 45 nm for  $\text{Cu}_{95}\text{Co}_5$ , compared to 62.5 nm for pure Cu and 75 nm for pure Co aerogels. This notable size reduction suggests that cobalt incorporation induces lattice strain that influences nanoparticle growth dynamics<sup>25</sup>. High-resolution transmission electron microscopy (HRTEM) analysis in Fig. 1c provides direct evidence of lattice parameter modifications. The measured interplanar spacing of 0.2188 nm corresponds to the (111) plane of face-centered cubic (fcc) Cu, representing an 11.22% contraction compared to standard Cu (0.2465 nm). Considering the slight difference in atomic radius between Cu (0.1278 nm) and Co (0.1253 nm), the resulting lattice distortion suggests that Co atoms are successfully incorporated into the Cu matrix, giving rise to a locally compressed Cu lattice environment.

Selected-area electron diffraction (SAED) patterns (Fig. 1d) confirm the coexistence of multiple crystalline phases, displaying diffraction rings indexed to CuO (111), Cu (111), Cu (200), Cu (220) and Cu(311) planes. X-ray diffraction (XRD) analysis (Fig. 1e) further elucidates the structural evolution. Pure Cu aerogel exhibits characteristic peaks for both metallic Cu (111, 200, 220) and CuO (111), while Co aerogel shows weak Co (111) diffraction intensity, suggesting poor crystallinity. Remarkably, the  $\text{Cu}_{95}\text{Co}_5$  aerogel pattern displays exclusively metallic Cu phases, indicating enhanced phase purity through Co doping. Notably, the Cu (111) peak position ( $42.8^\circ$ ) in  $\text{Cu}_{95}\text{Co}_5$  aerogel resides between those of pure Cu aerogel ( $43.3^\circ$ ) and Co aerogel ( $44.1^\circ$ ), with all diffraction peaks showing systematic high-angle shifts compared to pure Cu aerogel. This continuous peak shifting, accompanied by peak broadening, confirms lattice contraction induced by coherent incorporation of smaller Co atoms into the Cu matrix. Elemental distribution analysis through energy-dispersive X-ray spectroscopy (EDS) mapping (Fig. 1f) demonstrates homogeneous dispersion of Co species throughout the Cu matrix, as further supported by the EDS spectrum (Fig. S3). The absence of Co-rich clusters in EDS maps combined with uniform elemental distribution validates the formation of a solid solution structure rather than phase-segregated composites. Quantitative ICP-AES measurement (Fig. 1g, Table S1) confirms the actual Cu:Co ratio as 95.56:4.44, closely matching the nominal composition. Valence band spectroscopy (VBS) of X-ray photoelectron spectroscopy (XPS),

exhibiting particular sensitivity to d-orbitals near the Fermi level, enables reliable determination of the d-band center (Ed) through weighted averaging of background-subtracted spectral intensity (Shirley method)<sup>26-27</sup>. As shown in Fig. 1h,  $\text{Cu}_{95}\text{Co}_5$  aerogel demonstrates a notable Ed upshift of +0.03 eV versus pure Cu and +0.2 eV versus Co aerogels. This significant positive shift confirms synergistic electronic restructuring at the catalyst surface, directly attributable to atomic-level Co incorporation into the Cu lattice. The Cu aerogel exhibits characteristic Raman peaks at  $271\text{ cm}^{-1}$  ( $\text{F}_{2g}(1)$  lattice vibrations of Cu-O from defects/disorder in  $\text{Cu}_2\text{O}$ ),  $399\text{ cm}^{-1}$  ( $\text{A}_g$  or  $\text{B}_g$  modes associated with Cu-O bending vibrations in CuO),  $478\text{ cm}^{-1}$  ( $\text{A}_g$  symmetric stretching vibration of Cu-O in CuO) and  $728\text{ cm}^{-1}$  (Cu-OH bending, likely from residual hydroxides during freeze-drying) (Fig. S4). Co aerogel shows a distinct peak at  $646\text{ cm}^{-1}$  ( $\text{A}_{1g}$  symmetric Co-O stretching in  $\text{Co}_3\text{O}_4$ ). For  $\text{Cu}_{95}\text{Co}_5$  aerogel, the peaks at  $280\text{ cm}^{-1}$  ( $\text{F}_{2g}(1)$  Cu-O vibrations in  $\text{Cu}_2\text{O}$ ),  $331\text{ cm}^{-1}$  ( $\text{E}_g$  symmetric Co-O stretching in  $\text{Co}_3\text{O}_4$ ), and  $614\text{ cm}^{-1}$  ( $\text{A}_{1g}$ /defect-induced  $\text{Cu}_2\text{O}$  modes) confirm Cu-Co lattice interactions and defect-rich structures<sup>28-29</sup>.

### Nitrate Reduction Reaction ( $\text{NO}_3\text{RR}$ ) property

The electrocatalytic activity of the  $\text{Cu}_{95}\text{Co}_5$  aerogel toward  $\text{NO}_3\text{RR}$  was systematically investigated in a three-electrode H-cell configuration using 1 M KOH and 0.1 M  $\text{KNO}_3$  as the electrolyte. Linear sweep voltammetry (LSV) tests (Fig. 2a) revealed significantly enhanced geometric current densities for Cu aerogel, Co aerogel, and  $\text{Cu}_{95}\text{Co}_5$  aerogel catalysts in the presence of  $\text{KNO}_3$  compared to the  $\text{KNO}_3$  free electrolyte, confirming their preferential  $\text{NO}_3\text{RR}$  activity over the hydrogen evolution reaction (HER). While the onset potential ( $\sim 0.2\text{ V}$  vs. RHE) for  $\text{NO}_3\text{RR}$  remained comparable between Cu and  $\text{Cu}_{95}\text{Co}_5$  aerogels, Co doping markedly amplified the current density at identical potentials, with this enhancement becoming more pronounced at higher overpotentials. The LSV comparison among  $\text{Cu}_{95}\text{Co}_5$  aerogel,  $\text{Cu}_{99}\text{Co}_1$  aerogel, and  $\text{Cu}_{90}\text{Co}_{10}$  aerogel is presented in Fig. S5a. A volcano-shaped relationship between Co doping levels (1-10%) and  $\text{NO}_3\text{RR}$  performance was observed (Fig. S5b), where the  $\text{Cu}_{95}\text{Co}_5$  aerogel catalyst exhibited optimal activity, underscoring the critical role of doping concentration in modulating catalytic behavior. Further  $iR$ -corrected LSV analysis (Fig. S6) confirmed the superior onset potential and current density of  $\text{Cu}_{95}\text{Co}_5$  aerogel relative to pure Cu and Co aerogels, solidifying its exceptional  $\text{NO}_3\text{RR}$  capability.

XPS analysis (Fig. S7) demonstrates favorable electron redistribution between Co and Cu, and the electron transfer from Co to Cu facilitates interfacial charge transport. XPS quantification (Tables S2-3) shows a gradual decreasing in  $\text{Co}^0/\text{Co}$ , and increasing in  $\text{Cu}^+$  or  $\text{Cu}^0/\text{Cu}$  ratio. The higher Co doping levels suggests that Co incorporation effectively modifies the electronic environment of Cu, which modulates the d-band center and optimizes the adsorption energy of reaction intermediates, thereby enhancing catalytic performance. Electrochemical impedance spectroscopy (EIS) analysis (Fig. 2b) reveals that  $\text{Cu}_{95}\text{Co}_5$  aerogel exhibits the lowest charge transfer resistance ( $R_{ct}$ ) among the catalysts. Moreover,  $\text{Cu}_{95}\text{Co}_5$  aerogel maintains the smallest  $R_{ct}$  compared to  $\text{Cu}_{99}\text{Co}_1$  aerogel and  $\text{Cu}_{90}\text{Co}_{10}$  aerogel (Fig. S8),



indicating optimized reaction kinetics. Tafel slope analysis (Fig. S9)  $\text{Cu}_{95}\text{Co}_5$  ( $165 \text{ mV dec}^{-1}$ ), lower than those of pure Cu ( $263 \text{ mV dec}^{-1}$ ) and Co ( $275 \text{ mV dec}^{-1}$ ) aerogels, indicating accelerated reaction kinetics through Co-induced electronic modulation. It synergistically enhancing  $\text{NO}_3\text{RR}$  activity by accelerating charge transfer and optimizing intermediate adsorption energetics<sup>28</sup>.

Cyclic voltammetry (CV) measurements at varying scan rates ( $70\text{--}175 \text{ mV s}^{-1}$ ) enabled determination of double-layer capacitance ( $C_{dl}$ , Fig. S10), with  $\text{Cu}_{95}\text{Co}_5$  aerogel exhibiting the highest  $C_{dl}$  value ( $18.52 \text{ mF cm}^{-2}$ ) compared to Cu ( $16.96 \text{ mF cm}^{-2}$ )

performance enhancement arises from both increased active site exposure and optimized electronic properties.

Chronoamperometric (CA) tests were performed at applied potentials ranging from  $-0.3$  to  $-0.7 \text{ V}$  vs. RHE for 1 hour in  $40 \text{ mL}$  of  $0.1 \text{ M KNO}_3 + 1.0 \text{ M KOH}$  electrolyte to evaluate  $\text{NH}_3$  production rates and Faradaic efficiency (FE). Current-time profiles are provided in Fig. S13. Quantitative analysis of  $\text{NO}_2^-$  and  $\text{NH}_3$  concentrations was conducted via UV-vis spectroscopy using calibration curves (Figs. S14–15), while residual  $\text{NO}_3^-$  levels were determined via  $\text{NO}_3^-$  calibration curves (Figs. S16–17). Product distribution analysis revealed that  $\text{Cu}_{95}\text{Co}_5$  aerogel

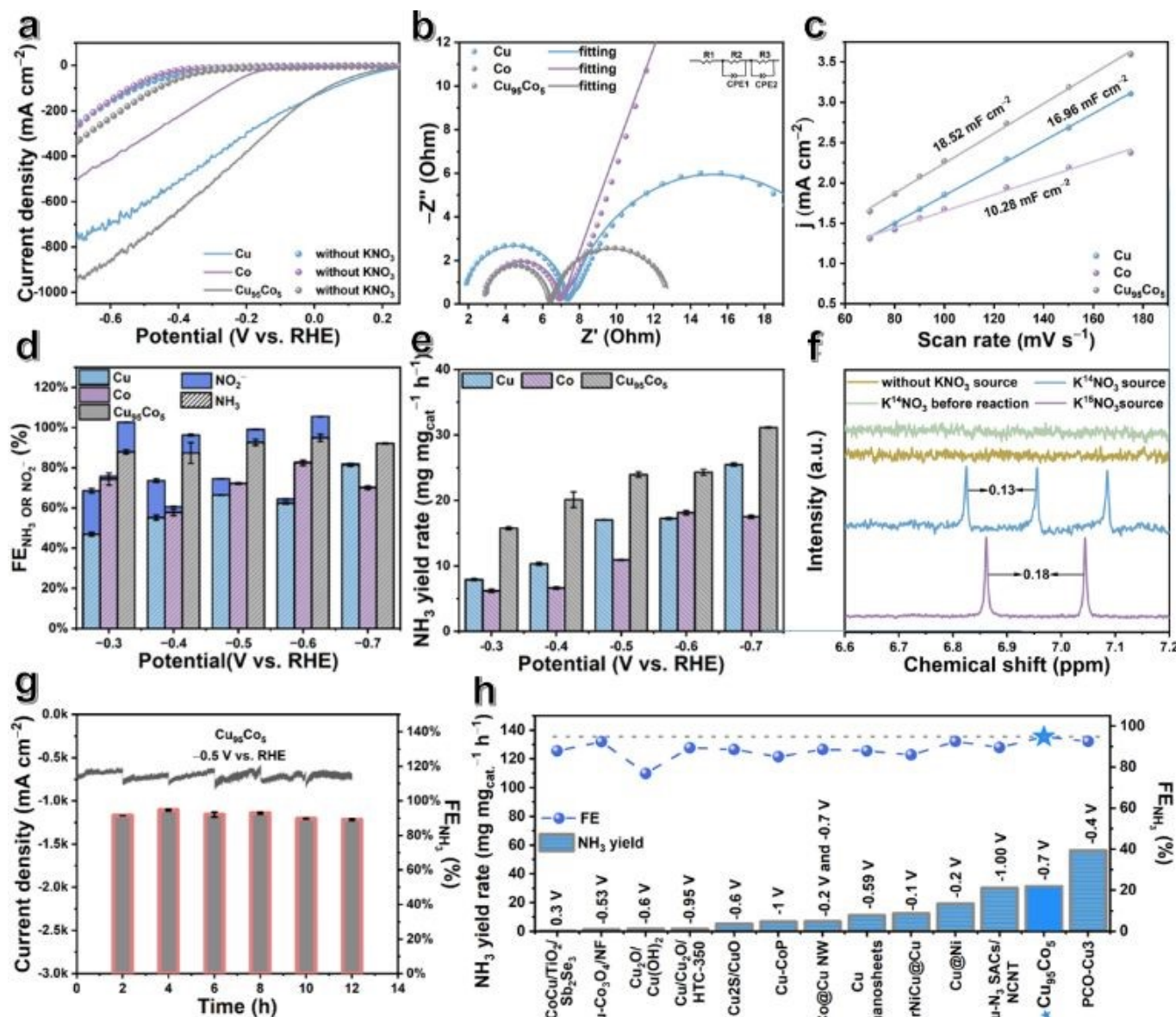


**Fig. 2** Electrocatalytic performance of  $\text{Cu}_{95}\text{Co}_5$  aerogel for  $\text{NO}_3\text{RR}$  conversion. (a) LSV curves of Cu aerogel, Co aerogel, and  $\text{Cu}_{95}\text{Co}_5$  aerogel catalysts in  $1 \text{ M KOH} + 0.1 \text{ M KNO}_3$  (without IR compensation). (b) Nyquist plots (EIS) at  $-1.0 \text{ V}$  versus Hg/HgO, with equivalent circuit model. (c) Double-layer capacitance ( $C_{dl}$ ) derived from capacitive current density ( $\Delta j = |j_a - j_c|$ ) at varying scan rates ( $70\text{--}175 \text{ mV s}^{-1}$ ). (d) Comparison of  $\text{FE}_{\text{NH}_3}$  and  $\text{FE}_{\text{NO}_2}$  of Cu aerogel, Co aerogel, and  $\text{Cu}_{95}\text{Co}_5$  aerogel catalysts ( $-0.3$  to  $-0.7 \text{ V}$  vs. RHE). (e) Comparison of  $\text{NH}_3$  yield rate of Cu aerogel, Co aerogel, and  $\text{Cu}_{95}\text{Co}_5$  aerogel catalysts. (f)  $^1\text{H}$  NMR spectra of the products produced after the electrocatalytic  $\text{NO}_3\text{RR}$  of  $\text{Cu}_{95}\text{Co}_5$  aerogel in the electrolyte of  $1 \text{ M KOH}$  without  $\text{KNO}_3$  (yellow line).  $^1\text{H}$  NMR of the fresh electrolytes before electrocatalytic reduction (marked as  $^{14}\text{NO}_3^-$ ) were provided as controls (green line).  $^1\text{H}$  NMR spectra of the products produced after the electrocatalytic  $\text{NO}_3\text{RR}$  of  $\text{Cu}_{95}\text{Co}_5$  aerogel in the electrolyte of  $1 \text{ M KOH}$  with  $0.1 \text{ M K}^{15}\text{NO}_3$  and  $0.1 \text{ M K}^{14}\text{NO}_3$  at  $-0.7 \text{ V}$  (V vs. RHE) (blue and purple lines). (g) Cyclic stability test:  $\text{FE}_{\text{NH}_3}$  and  $\text{NH}_3$  yield rates over 12 hours (6 cycles, 2 h/cycle) with electrolyte replenishment every 2 h. (h) Comparison of the  $\text{NH}_3$  yield rate of  $\text{Cu}_{95}\text{Co}_5$  aerogel at the potential of  $-0.7 \text{ V}$  (V vs. RHE) for 1 h of electrocatalytic  $\text{NO}_3\text{RR}$  with other reported catalysts.





and Cu<sub>90</sub>Co<sub>10</sub> aerogel) at all potentials (Fig. S18b), achieving a remarkable production rate of  $31.15 \pm 0.086 \text{ mg mg}_{\text{cat}}^{-1} \text{ cm}^{-2} \text{ h}^{-1}$  at  $-0.7 \text{ V}$  (Fig. 2e). A peak energy efficiency (EE) of  $31.03 \pm 0.0039\%$  was achieved for NH<sub>3</sub> synthesis over the

Cu<sub>95</sub>Co<sub>5</sub> aerogel, at an applied potential of  $-0.3 \text{ V}$  versus RHE (Fig. S19). With the nitrate reduction reaction (NO<sub>3</sub>RR) advancing toward industrial implementation<sup>31</sup>, the cost of ammonia (NH<sub>3</sub>) production has become a key performance

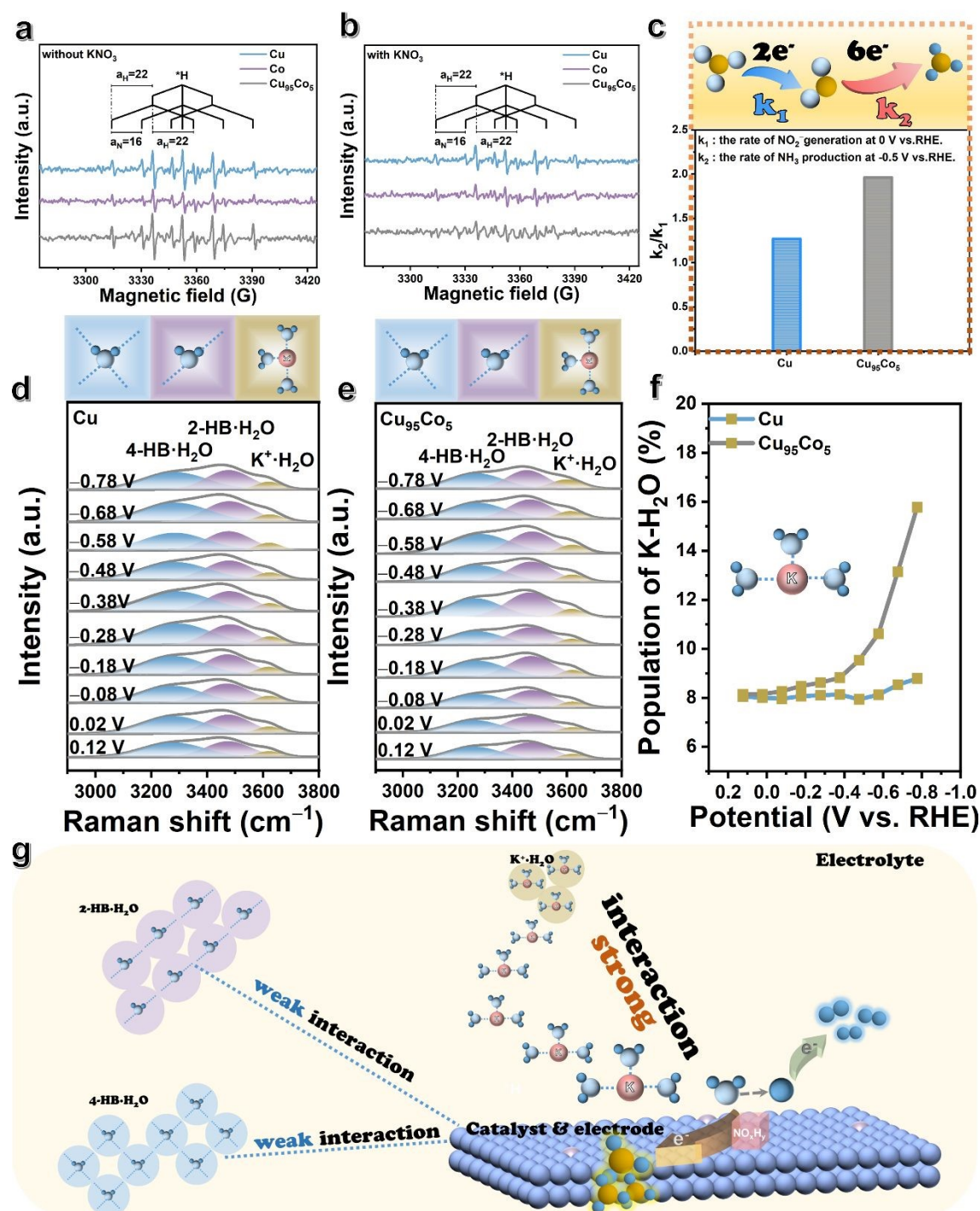


**Fig. 3** Characterization of protonic hydrogen in NO<sub>3</sub>RR. (a-b) EPR spectra of the electrolyte for Cu aerogel, Co aerogel and Cu<sub>95</sub>Co<sub>5</sub> aerogel in 1 M KOH and 1 M KOH with 0.1 M KNO<sub>3</sub>. (c) The  $k_2/k_1$  ratios of Cu aerogel and Cu<sub>95</sub>Co<sub>5</sub> aerogel catalysts during NO<sub>3</sub>RR. Potential dependent in situ SERS of interfacial water on (d) Cu and (e) Cu<sub>95</sub>Co<sub>5</sub> electrode surface during NO<sub>3</sub>RR process. Gaussian fits of three O-H stretching models of 4-HB·H<sub>2</sub>O, 2-HB·H<sub>2</sub>O, and K<sup>+</sup>·H<sub>2</sub>O are shown in blue, purple and green. (f) Estimated proportions of K<sup>+</sup>·H<sub>2</sub>O based on the peak areas of the green bands in the 2900-3800 cm<sup>-1</sup> Raman spectra on the surfaces of Cu (blue lines) and Cu<sub>95</sub>Co<sub>5</sub> (green lines). (g) Schematic illustration of the mechanism by which Cu<sub>95</sub>Co<sub>5</sub> aerogel facilitates interfacial water splitting to provide protonic hydrogen, thereby promoting the nitrate reduction reaction.



metric with significant economic implications. Based solely on the cost of renewable electricity ( $\$0.03 \text{ kWh}^{-1}$ ), the  $\text{Cu}_{95}\text{Co}_5$  aerogel catalyst enables an energy consumption of  $17.82 \pm 0.22 \text{ kWh kg}^{-1} \text{ NH}_3$ , corresponding to a remarkably low production cost of  $\text{US}\$0.53 \pm 0.0066 \text{ kg}^{-1} \text{ NH}_3$ —substantially below the current commercial price of  $\text{NH}_3$  (approximately  $\$1.0\text{--}1.5 \text{ kg}^{-1}$ ). In addition, raw material cost estimation suggests that the  $\text{Cu}_{95}\text{Co}_5$  aerogel can be synthesized at a cost of less than  $\$1,300$  per kilogram, further underscoring its economic advantage over noble-metal-based catalysts. This substantial cost advantage highlights the economic viability of electrocatalytic  $\text{NO}_3\text{RR}$  as a sustainable alternative to the traditional Haber-Bosch process. Moreover, long-term chronoamperometry tests reveal that the catalyst exhibits a stable lifetime of at least 36 h (Fig. S20). It should be noted that this cost estimation is simplified, considering electricity price only, and does not account for capital expenditures or Ohmic losses. Nevertheless, when combined with the environmental benefits of nitrate remediation, the  $\text{Cu}_{95}\text{Co}_5$  aerogel catalyst emerges as a highly attractive candidate for scalable and economically competitive  $\text{NO}_3\text{RR}$ . Its EE was further benchmarked against those of recently reported catalysts (Table S4). The  $\text{NH}_3$  partial current density  $j_{\text{NH}_3}$  of  $\text{Cu}_{95}\text{Co}_5$  aerogel further confirms its enhanced activity (Fig. S20).

We have conducted rigorous control experiments to unequivocally confirm the origin of  $\text{NH}_3$ :  $^1\text{H}$  NMR analysis of post-electrolysis  $\text{KNO}_3$ -free electrolyte (1 M KOH,  $-0.7 \text{ V}$  vs. RHE, 1 h) detected no  $\text{NH}_3$  signal, confirming that  $\text{NH}_3$  formation absolutely requires  $\text{NO}_3^-$  as the reactant (Fig. S21).  $^1\text{H}$  NMR spectra of products from  $^{15}\text{N}$  isotope labeling  $^{15}\text{NO}_3^-$  electrolyte exhibit the characteristic doublet of  $^{15}\text{NH}_3$ , while  $^{14}\text{NO}_3^-$  yields the triplet of  $^{14}\text{NH}_3$  (Fig. 2f). This definitively traces the nitrogen source to electrolyte-derived  $\text{NO}_3^-$ , eliminating contributions from catalyst decomposition, atmospheric  $\text{N}_2$ , or environmental contamination<sup>22</sup>.

Cyclic stability tests at  $-0.5 \text{ V}$  vs. RHE (6 cycles, 2 h/cycle) demonstrated robust performance retention, with  $\text{FE}_{\text{NH}_3}$  sustained at  $\sim 90\%$  and negligible current density decay (Fig. 2g). Extended 36-hour operation with electrolyte replenishment every 12 h revealed stable  $\text{NH}_3$  production ( $\text{FE} > 70\%$ , Fig. S22). We have conducted comprehensive post-electrolysis characterization after both 12-hour and 36-hour chronoamperometry tests, including TEM, XRD, XPS, and ICP analyses to evaluate morphological, structural, and compositional changes. As shown in Fig. S23 (TEM images), the catalyst largely maintained its overall morphology after 12 hours of operation, with no significant structural degradation observed. However, after 36 hours, while the majority of nanoparticles retained their original size and shape, the appearance of needle-shaped nanoparticles indicates certain morphological evolution under extended operation. XRD analysis (Fig. S24) reveals that the characteristic (111), (200), and (220) crystal planes of  $\text{Cu}_{95}\text{Co}_5$  remained intact after both 12-hour and 36-hour tests, confirming the preservation of bulk crystal structure. After 12 hours, weak CuO (11-1)/(111) peaks emerged ( $36\text{--}37^\circ$ ), suggesting minor surface oxidation in alkaline media. After 36 hours, these CuO peaks intensified

while the signal-to-noise ratio decreased, indicating both enhanced surface oxidation and some crystal quality deterioration. XPS analysis (Fig. S25) demonstrates that the Cu/Co oxidation states remained essentially unchanged after 12 hours of operation. After 36 hours, the spectra remained similar. The overall chemical states maintained well, confirming remarkable structural integrity. ICP results (Fig. S26) show that the Co/Cu ratio decreased slightly from 4.44% to 3.43% after 36 hours, suggesting minor Co leaching during prolonged operation. In summary, these multi-technique analyses demonstrate that  $\text{Cu}_{95}\text{Co}_5$  aerogel maintains excellent electrochemical and structural stability during 12-hour operation, and largely preserves its fundamental properties even after extended 36-hour testing, with only minimal surface oxidation and negligible Co leaching. As summarized in Fig. 2h and Table S5,  $\text{Cu}_{95}\text{Co}_5$  aerogel outperforms most previously reported catalysts in both  $\text{NH}_3$  yield and FE attributed to its optimized electronic structure (Co-induced Cu lattice strain) and hierarchical porosity, which synergistically enhance  $\text{NO}_3^-$  adsorption, intermediate stabilization, and  $\text{NH}_3$  desorption. These results establish  $\text{Cu}_{95}\text{Co}_5$  aerogel as a benchmark catalyst for efficient nitrate-to-ammonia conversion. And this approach represents a promising strategy for enhancing the performance  $\text{NO}_3\text{RR}$  catalysts through rational heteroatom doping and nanostructure engineering.

#### Mechanistic Study of Catalysts in $\text{NO}_3\text{RR}$

To probe the Cu-Co electronic interplay and its impact on active hydrogen ( $^*\text{H}$ ) generation, CV in 1 M KOH revealed distinct hydrogen evolution reaction (HER) features. As shown in Fig. S27a,  $\text{Cu}_{95}\text{Co}_5$  aerogel exhibits a pronounced HER region below  $0.35 \text{ V}$  vs. RHE, with hydrogen adsorption spanning  $0.32$  to  $-0.19 \text{ V}$ . Both Cu aerogel and  $\text{Cu}_{95}\text{Co}_5$  aerogel display similar low-potential hydrogen adsorption (Fig. S27b), whereas Co shows no such activity (Fig. S28c)<sup>32</sup>. To quantify  $^*\text{H}$  generation/consumption during  $\text{NO}_3\text{RR}$ , electrochemical quasi-in situ electron paramagnetic resonance (EPR) measurements were conducted in 1.0 M KOH with/without 0.1 M  $\text{KNO}_3$  at  $-0.6 \text{ V}$  vs. RHE for 5 min, using 5,5-dimethyl-1-pyrroline N-oxide (DMPO) as a spin trap. In  $\text{KNO}_3$  free electrolyte,  $\text{Cu}_{95}\text{Co}_5$  aerogel generates a nine-line EPR spectrum (intensity ratio  $\sim 1:1:2:1:2:1:2:1:1$ , Fig. 3a), characteristic of DMPO- $^*\text{H}$  adducts, confirming efficient  $^*\text{H}$  production via water dissociation. As shown in Fig. 3b, monometallic Cu aerogel and Co aerogel exhibit weaker signals, indicating inferior HER activity. Upon introducing 0.1 M  $\text{KNO}_3$ ,  $\text{Cu}_{95}\text{Co}_5$  aerogel shows a marked reduction in DMPO- $^*\text{H}$  signal intensity, attributed to rapid  $^*\text{H}$  consumption by  $\text{NO}_3\text{RR}$  intermediates, thereby promoting stepwise  $\text{NO}_3^-$  hydrogenation. In contrast, the relatively small signal attenuation observed for monometallic catalysts indicates their lower  $^*\text{H}$  utilization efficiency. This limitation is most likely





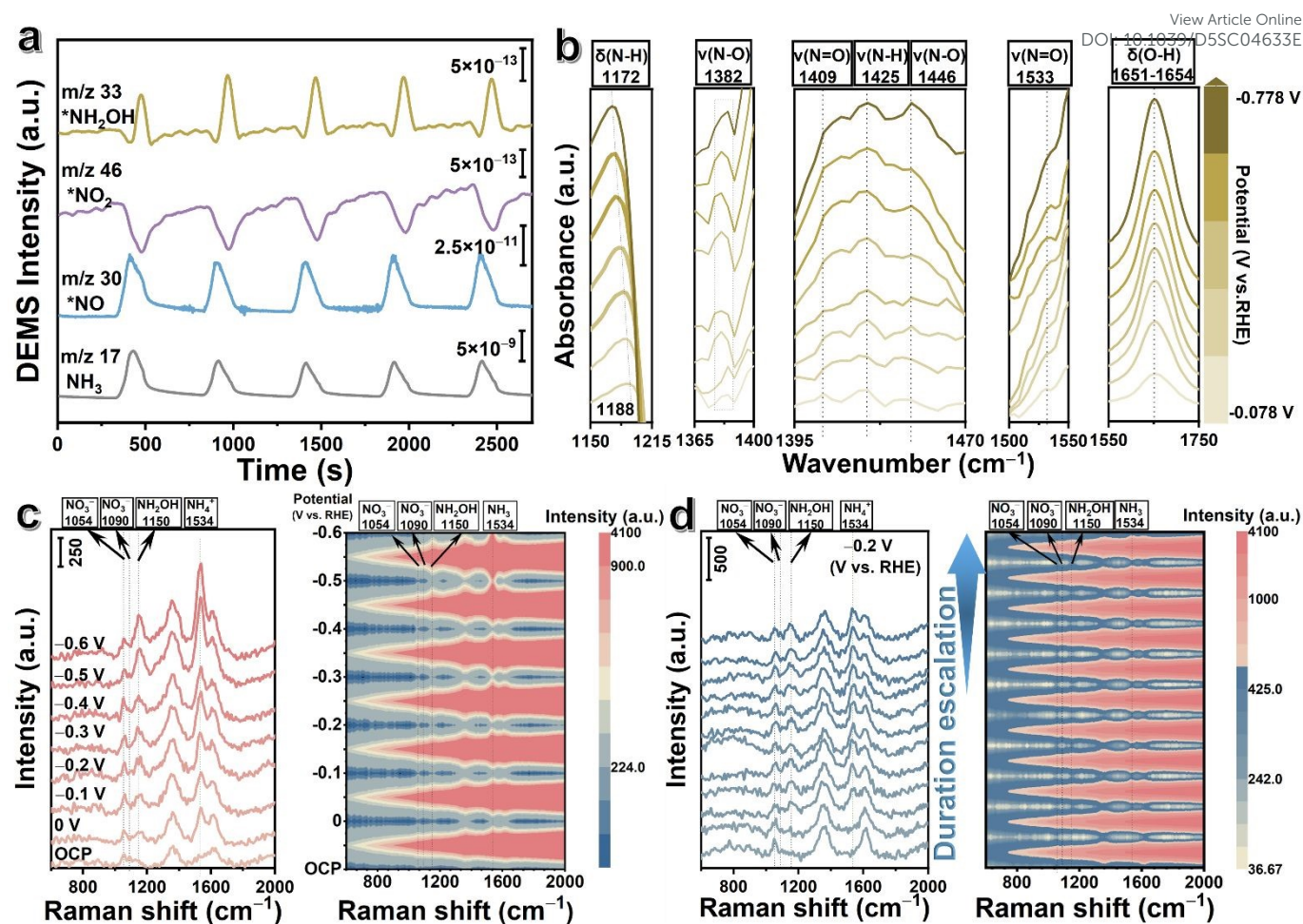


**Fig. 4** Characterization of NO<sub>3</sub>RR Reaction Pathways. (a) Electrochemical online DEMS results for the NO<sub>3</sub>RR over Cu<sub>95</sub>Co<sub>5</sub> aerogel. (b) Electrochemical in situ ATR-FTIR spectra of NO<sub>3</sub>RR over Cu<sub>95</sub>Co<sub>5</sub> aerogel at different potentials from -0.078 to -0.778 V vs. RHE. (c) In situ Raman spectra during the electrocatalytic nitrate reduction process using Cu<sub>95</sub>Co<sub>5</sub> aerogel as the catalyst, showing changes with negative potential shifts (from 0 to -0.6 V vs. RHE). (Assignments: δ - bending vibration; ν - stretching vibration; ν<sub>s</sub> - symmetric stretching; ν<sub>as</sub> - asymmetric stretching). The corresponding counter plot is also provided. (d) In situ Raman spectra during the electrocatalytic nitrate reduction process using Cu<sub>95</sub>Co<sub>5</sub> aerogel as the catalyst, showing changes over time. The corresponding counter plot is also provided.

associated with their restricted ability to supply proton-derived hydrogen species, which hinders the effective formation and participation of reactive hydrogen intermediates during catalysis. These results underscore that Cu-Co synergy enhances \*H generation efficiency and facilitates its dynamic transfer to reaction intermediates, accelerating NO<sub>3</sub><sup>-</sup> to NH<sub>3</sub> kinetics and improving overall NO<sub>3</sub>RR selectivity. The tailored electronic structure of Cu<sub>95</sub>Co<sub>5</sub> aerogel optimizes \*H availability while suppressing competitive HER, establishing a mechanistic foundation for its superior catalytic performance.

#### Kinetic

Comparative linear sweep voltammetry (LSV) of NO<sub>3</sub>RR and NO<sub>2</sub>RR (Fig. S28) revealed a negative shift in onset potential for Cu (-0.04 V vs. RHE) and Cu<sub>95</sub>Co<sub>5</sub> (-0.04 V) compared to Co (-0.13 V), indicating Co's inferior NO<sub>3</sub><sup>-</sup> → NO<sub>2</sub><sup>-</sup> kinetics. Product analysis (Figs. S29a-b) showed Cu<sub>95</sub>Co<sub>5</sub> achieves >93% FE<sub>NH<sub>3</sub></sub> and 40.08 ± 0.82 mg mg<sub>cat</sub><sup>-1</sup> h<sup>-1</sup> NH<sub>3</sub> yield in NO<sub>2</sub>RR, outperforming Cu (37.21 ± 0.42 mg mg<sub>cat</sub><sup>-1</sup> h<sup>-1</sup>) and Co (35.96 ± 0.60 mg mg<sub>cat</sub><sup>-1</sup> h<sup>-1</sup>). The Faradaic efficiency (FE) and product yield at 0 V are shown in Fig. S30 and rate constants (k<sub>1</sub> for NO<sub>3</sub><sup>-</sup> → NO<sub>2</sub><sup>-</sup>, k<sub>2</sub> for NO<sub>2</sub><sup>-</sup> → NH<sub>3</sub>) quantified via

electrochemical analysis (Table S6) revealed Cu<sub>95</sub>Co<sub>5</sub>'s superior k<sub>2</sub> (0.11 h<sup>-1</sup> vs. 0.07 h<sup>-1</sup> for Cu). The k<sub>2</sub>/k<sub>1</sub> ratio (2.34 for Cu<sub>95</sub>Co<sub>5</sub> vs. 1.77 for Cu, Fig. 3c) highlights Co doping's preferential enhancement of NO<sub>2</sub><sup>-</sup> → NH<sub>3</sub> hydrogenation<sup>24</sup>. Concentration-dependent studies (Fig. S31) demonstrated optimal NH<sub>3</sub> yield at 0.1 M NO<sub>3</sub><sup>-</sup>, with performance decline at ≥ 0.2 M due to limited proton supply or altered electron pathways. Below 0.05 M NO<sub>3</sub><sup>-</sup>, the balance between NO<sub>3</sub><sup>-</sup> → NO<sub>2</sub><sup>-</sup> rate and \*H availability dictates overall efficiency. Co doping enhances \*H generation, optimizing NO<sub>2</sub><sup>-</sup> → NH<sub>3</sub> kinetics while Cu sites stabilize intermediates. This synergy enables efficient eight-electron conversion (94.91 ± 0.018% FE, 31.15 ± 0.086 mg mg<sub>cat</sub><sup>-1</sup> h<sup>-1</sup>), establishing Cu<sub>95</sub>Co<sub>5</sub> aerogel as a benchmark catalyst for nitrate-to-ammonia electrocatalysis.

#### K<sup>+</sup>-H<sub>2</sub>O Regulation

In alkaline electrolyte, the protons (H<sup>+</sup>) required for the nitrate reduction reaction (NO<sub>3</sub>RR) primarily originate from the interfacial water adsorbed on the surface of the catalyst<sup>32-34</sup>. To further explore how Co doping imparts superior NO<sub>3</sub>RR kinetics to the Cu<sub>95</sub>Co<sub>5</sub> catalyst compared to the monometallic Cu, we employed in situ SERS (Figs. 3d-e) to analyze the interfacial water structure on the Cu





aerogel and Cu<sub>95</sub>Co<sub>5</sub> aerogel electrode surfaces. (The schematic diagram of the in situ electrochemical testing reactor is presented in Fig. S32.) Through Gaussian fitting, we identified three main components of interfacial water: tetra-coordinated hydrogen-bonded water (4-HB-H<sub>2</sub>O), bi-coordinated hydrogen-bonded water (2-HB-H<sub>2</sub>O), and hydrated potassium ion water (K<sup>+</sup>-H<sub>2</sub>O). Among them, K<sup>+</sup>-H<sub>2</sub>O, which forms weak hydrogen bonds with 2-HB-H<sub>2</sub>O, is more easily dissociated, thereby accelerating proton transfer. Fig. 3f shows the variation of K<sup>+</sup>-H<sub>2</sub>O content with potential at the interfaces of Cu aerogel and Cu<sub>95</sub>Co<sub>5</sub> aerogel catalysts (the trends for 4-HB-H<sub>2</sub>O and 2-HB-H<sub>2</sub>O are shown in Supporting Information, Fig. S33). K<sup>+</sup>-H<sub>2</sub>O is closely related to both the water dissociation ability and the generation of active hydrogen (H<sup>\*</sup>). The results indicate that, on the Cu<sub>95</sub>Co<sub>5</sub> aerogel catalyst surface, the proportion of K<sup>+</sup>-H<sub>2</sub>O increases significantly from 8.15% to 15.78%. In contrast, on the Cu aerogel catalyst surface, the content of K<sup>+</sup>-H<sub>2</sub>O remains relatively low and shows minimal change, increasing slightly from 8.05% to 8.79%. This comparison suggests that, compared to Cu aerogel, Cu<sub>95</sub>Co<sub>5</sub> aerogel has a stronger water dissociation capability, generating more active hydrogen (H<sup>\*</sup>), and the supply rate of H<sup>\*</sup> is more closely matched with the rate of the NO<sub>3</sub><sup>-</sup> → NO<sub>2</sub><sup>-</sup> reaction<sup>15,27</sup>. Additionally, as shown in Supporting Information, Fig. S34, the Raman peak of K<sup>+</sup>-H<sub>2</sub>O also shows a more pronounced low-wavenumber shift for Cu<sub>95</sub>Co<sub>5</sub> compared to Cu, further proving that K<sup>+</sup>-H<sub>2</sub>O at the Cu<sub>95</sub>Co<sub>5</sub> aerogel interface is subject to stronger electronic modulation<sup>15</sup>. During nitrate reduction (NO<sub>3</sub>RR), the availability of active hydrogen (H<sup>\*</sup>) plays a pivotal role in determining both the reaction selectivity and the Faradaic efficiency (FE). An insufficient H<sup>\*</sup> supply can limit the overall reduction process, while an excessive H<sup>\*</sup> presence may promote competing side reactions, thereby lowering the Faradaic efficiency toward ammonia (NH<sub>3</sub>). Moderate Co doping can enhance water dissociation by regulating the interfacial water structure and increasing the concentration of K<sup>+</sup>-H<sub>2</sub>O, i.e., the concentration of easily disrupted hydrogen bond networks, thereby promoting H<sup>\*</sup> generation and improving catalyst activity (Fig. 3g). This mechanism helps optimize the kinetic matching between the NO<sub>3</sub><sup>-</sup> → NO<sub>2</sub><sup>-</sup> and NO<sub>2</sub><sup>-</sup> → \*NH<sub>3</sub> reaction steps, leading to the superior catalytic performance of Cu<sub>95</sub>Co<sub>5</sub> aerogel in NO<sub>3</sub>RR.

### In Situ Probing of NO<sub>3</sub>RR Pathways

Differential electrochemical mass spectrometry (DEMS) was employed to monitor key reaction intermediates during the electrocatalytic nitrate reduction reaction (NO<sub>3</sub>RR) by detecting characteristic mass-to-charge ratios (\*m/z\*): \*m/z\* = 33 (\*NH<sub>2</sub>OH\*), \*m/z\* = 46 (\*NO<sub>2</sub><sup>-</sup>), \*m/z\* = 30 (\*NO\*), and \*m/z\* = 17 (\*NH<sub>3</sub>\*) (Fig. 4a). The relative intensity of the detected species followed the order: NH<sub>3</sub> > NO > NH<sub>2</sub>OH > NO<sub>2</sub><sup>-</sup>, indicating a progressive hydrogenation pathway and consumption of nitrogen-oxygen intermediates. Complementary linear sweep voltammetry (LSV) data (Fig. S35) confirmed the potential-dependent evolution of NH<sub>3</sub>, demonstrating a gradual increase in the \*m/z\* = 17 signal intensity under reductive conditions<sup>21, 25</sup>. This trend aligns with the cumulative formation of NH<sub>3</sub> through multi-step proton-coupled electron transfers. These DEMS and LSV results collectively demonstrate the sequence \*NO<sub>3</sub><sup>-</sup> → \*NO<sub>2</sub><sup>-</sup> → \*NO → \*NH<sub>2</sub>OH → NH<sub>3</sub> is supported by the

temporal evolution of intermediate signals. The dominant NH<sub>3</sub> signal indicates high selectivity toward ammonia formation over competing pathways.

To elucidate the stepwise conversion of \*NO<sub>3</sub> to \*NH<sub>3</sub>, in situ attenuated total reflection Fourier-transform infrared (ATR-FTIR) spectroscopy was conducted over Cu<sub>95</sub>Co<sub>5</sub> aerogel catalysts from -0.078 to -0.778 V vs. RHE to resolve the NO<sub>3</sub>RR pathway (Fig. 4b). The distinct absorption band at 1172 cm<sup>-1</sup> is assigned to the N-H bending vibration (δN-H) of adsorbed hydroxylamine (\*NH<sub>2</sub>OH\*), confirming its pivotal role as a key intermediate. The peak at 1382 cm<sup>-1</sup> corresponds to the symmetric N-O stretching vibration (ν<sub>s</sub>N-O) of surface-adsorbed nitrate (\*NO<sub>3</sub>), indicative of its initial adsorption and activation at Cu sites. Concurrently, the signal at 1409 cm<sup>-1</sup> is attributed to the N=O stretching vibration (νN=O) of adsorbed nitrite (\*NO<sub>2</sub><sup>-</sup>), highlighting its role as an early intermediate. The peak at 1425 cm<sup>-1</sup> arises from the N-H stretching vibration (νN-H) of \*NH<sub>2</sub> intermediates, while the feature at 1446 cm<sup>-1</sup> is assigned to the symmetric N-O stretch (ν<sub>s</sub>N-O) of \*NO<sub>2</sub><sup>-</sup>, evidencing its involvement in subsequent deoxygenation steps. Additionally, the absorption band at 1533 cm<sup>-1</sup> is ascribed to the asymmetric N=O stretching vibration (ν<sub>as</sub>N=O) of adsorbed \*NO or \*NO<sub>2</sub> species, supporting the progressive reduction of nitrogen-oxygen intermediates. A broad peak near 1651 cm<sup>-1</sup>, attributed to N-H/O-H bending modes (δN-H/δO-H), likely originates from \*NH<sub>2</sub>OH or interfacial water molecules, a key intermediate formed through two consecutive hydrogenation steps of the \*NOH species at the nitrogen site. These spectroscopic signatures collectively validate the existence and transformation of critical intermediates (\*NO<sub>3</sub>, \*NO<sub>2</sub>, \*NO, \*NH<sub>2</sub>OH) and elucidate a sequential reaction pathway mediated by Cu-Co synergy: (1) nitrate adsorption/activation, (2) stepwise deoxygenation (\*NO<sub>3</sub> → \*NO<sub>2</sub> → \*NO), and (3) hydrogenation (\*NO → \*NH<sub>2</sub>OH → \*NH<sub>3</sub>)<sup>24, 26-28</sup>. The Cu sites facilitate nitrate adsorption and initial activation, while Co doping enhances H<sup>\*</sup> transfer efficiency, stabilizing intermediates and accelerating electron transfer. This synergistic interplay optimizes the balance between deoxygenation kinetics and hydrogenation thermodynamics, enabling efficient eight-electron nitrate-to-ammonia conversion.

Complementary to Raman spectroscopy, electrochemical-SERS monitoring was performed using Cu<sub>95</sub>Co<sub>5</sub> aerogel as the SERS substrate across 600-2000 cm<sup>-1</sup>. As depicted in Fig. 4c, the distinct peak at 1054 cm<sup>-1</sup> is assigned to the vibrational mode of adsorbed nitrate (\*NO<sub>3</sub>), indicative of its adsorption and activation on the catalyst surface. At -0.2 V vs. RHE, time-dependent SERS measurements revealed the emergence of three characteristic peaks: 1090 cm<sup>-1</sup> (N-O stretching vibration of \*NO<sub>3</sub>), 1150 cm<sup>-1</sup> (N-H bending of \*NH<sub>2</sub>OH), and 1534 cm<sup>-1</sup> (N-H stretching of \*NH<sub>3</sub>). The sequential appearance and intensification of these peaks<sup>22,35-36</sup>, confirm the progressive hydrogenation pathway: \*NO<sub>3</sub> → \*NH<sub>2</sub>OH → \*NH<sub>3</sub>. Potential-dependent in situ SERS studies (0 to -0.6 V vs. RHE, Fig. 4d) demonstrated that the intensities of 1150 cm<sup>-1</sup> (\*NH<sub>2</sub>OH) and 1534 cm<sup>-1</sup> (\*NH<sub>3</sub>) peaks increased significantly at more negative potentials, reflecting enhanced intermediate formation and product generation under higher overpotentials.



DFT Insights into NO<sub>3</sub>RR Mechanism on Cu<sub>95</sub>Co<sub>5</sub> Aerogel

hydrogenation on adjacent Co sites. This mechanism, driven by

DOI: 10.1039/D5SC04633E

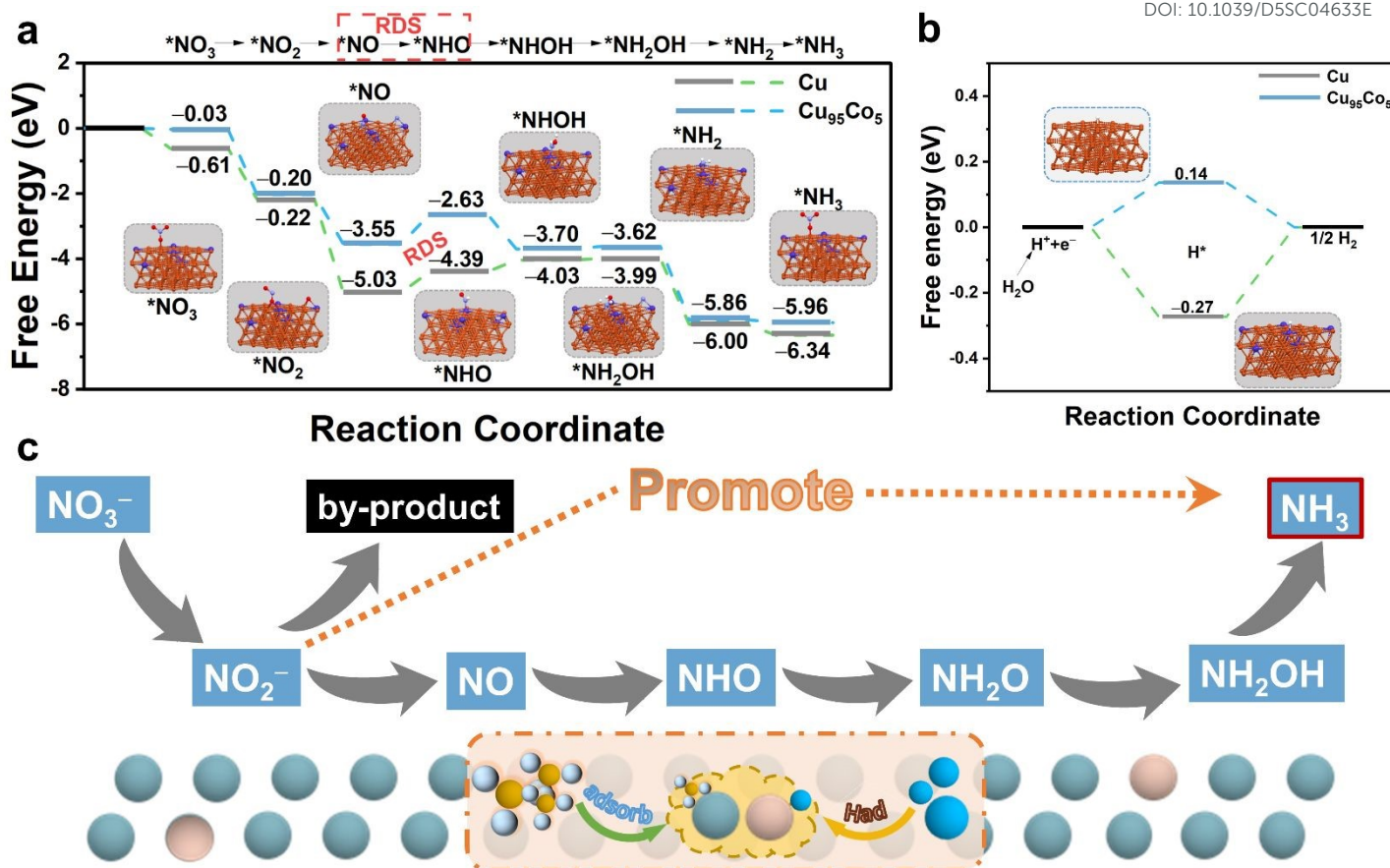


**Fig. 5** Density functional theory calculations of the Gibbs free energy diagram for NO<sub>3</sub><sup>-</sup> reduction reaction (NO<sub>3</sub>RR) and \*H adsorption on the Cu<sub>95</sub>Co<sub>5</sub> surface. (a) Free energy profiles of the NO<sub>3</sub>RR intermediate steps (inset: stable adsorption configurations of the reaction intermediates). (b) Free energy profile of \*H adsorption on the Cu<sub>95</sub>Co<sub>5</sub> surface. (c) NO<sub>3</sub><sup>-</sup> reduction pathway during NO<sub>3</sub>RR using Cu<sub>95</sub>Co<sub>5</sub> aerogel as the catalyst.

To elucidate the reaction mechanism and the role of Co doping at the atomic level, we performed comprehensive density functional theory (DFT) calculations on the Cu<sub>95</sub>Co<sub>5</sub> system, focusing on the gradual deoxygenation and subsequent hydrogenation steps. As shown in Fig. 5a, the optimized configurations of key intermediates and the corresponding Gibbs free energy profiles reveal that the rate-determining step (RDS) is the hydrogenation of \*NO to \*NHO. The RDS is defined as the elementary reaction step with the highest energy barrier controlling the overall reaction kinetics, exhibits a significantly lower barrier on Cu<sub>95</sub>Co<sub>5</sub> (0.64 eV) compared to pure Cu (0.92 eV). Further analysis of the \*H adsorption free energy (Fig. 5b) demonstrates that Cu<sub>95</sub>Co<sub>5</sub> possesses stronger \*H binding affinity than pure Cu, which accounts for the reduced energy barrier during the \*NO → \*NHO conversion. This computational finding aligns consistently with our operando SERS results, which confirmed enhanced interfacial water dissociation and increased \*H availability on the Co-doped surface. Integrating these DFT results with multimodal experimental evidence—including DEMS, in-situ FT-ATIR, <sup>1</sup>H NMR, and in-situ SERS spectroscopy—we propose a synergistic dual-site mechanism (Fig. 5c): NO<sub>3</sub><sup>-</sup> is preferentially adsorbed and reduced to NO<sub>2</sub><sup>-</sup> on Cu sites, facilitated by favorable electronic interactions, followed by desorption and subsequent

mutual electronic modulation between Cu and Co, enables efficient nitrate-to-ammonia conversion through optimized intermediate stabilization and hydrogenation kinetics.

#### Zinc-Nitrate (Zn-NO<sub>3</sub><sup>-</sup>) Battery System

The zinc-nitrate (Zn-NO<sub>3</sub><sup>-</sup>) battery is an environmentally friendly and efficient clean energy conversion system that can convert NO<sub>3</sub><sup>-</sup> in wastewater into high-value products, such as NH<sub>3</sub>, while providing power<sup>2</sup>. During the discharge process, zinc dissolves at the anode, while NO<sub>3</sub>RR is catalyzed at the cathode. Since the reduction of NO<sub>3</sub><sup>-</sup> to NH<sub>3</sub> involves a complex 8-electron transfer process, this system provides sufficient electron flow to ensure stable battery output and efficient energy utilization. Given the excellent catalytic activity of Cu<sub>95</sub>Co<sub>5</sub> in the NO<sub>3</sub>RR, it was used as the cathode, and zinc foil was selected as the anode to construct the Zn-NO<sub>3</sub><sup>-</sup> battery shown in Fig. 6a. As shown in Fig. 6b, the Zn-NO<sub>3</sub><sup>-</sup> battery with Cu<sub>95</sub>Co<sub>5</sub> as the catalytic cathode exhibits an open-circuit voltage of 1.49 V, which remains stable for 1 hour, indicating good electrochemical stability. Power density is one of the key indicators of battery performance and is crucial for evaluating energy conversion efficiency and practical application potential. As shown in Fig. 6c, the Zn-NO<sub>3</sub><sup>-</sup> battery based on Cu<sub>95</sub>Co<sub>5</sub> reaches a maximum power density of 12.40 mW cm<sup>-2</sup> at 0.35 V (V vs. Zn). Additionally, as shown in Fig. 6d, this Zn-NO<sub>3</sub><sup>-</sup> battery



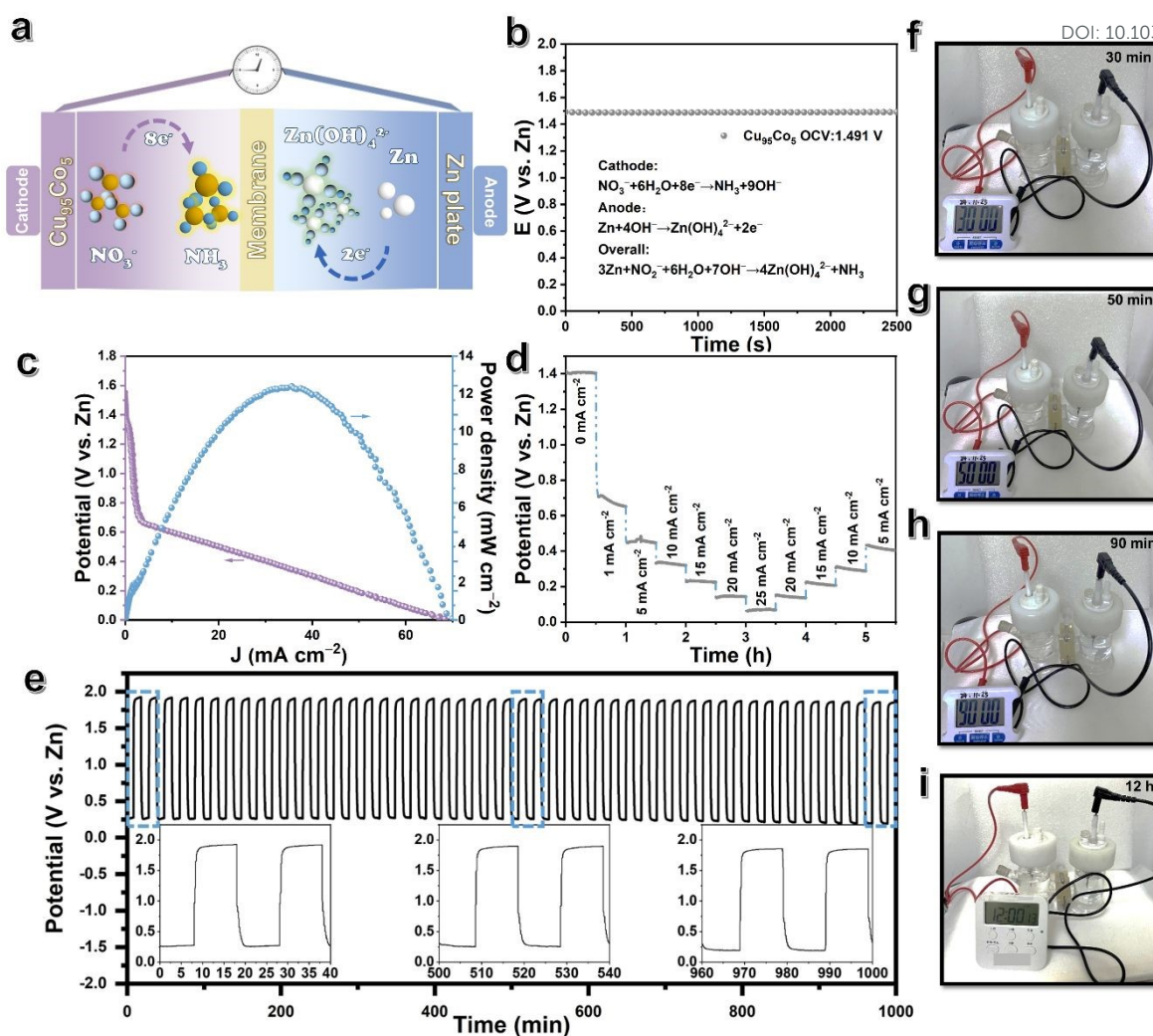


**Fig. 6** Zn-NO<sub>3</sub><sup>-</sup> Battery. NO<sub>3</sub>RR-involved rechargeable hybrid battery measurements. (a) Schematic diagram of rechargeable Zn-NO<sub>3</sub><sup>-</sup> battery. (b) Open-circuit voltage tests, (c) polarization curve and power density tests, and (d) multi-step chronoamperometric curves of Cu<sub>95</sub>Co<sub>5</sub> aerogel cathodes at various current densities during the discharge process. (e) Long-term cycling stability test of Zn-NO<sub>3</sub><sup>-</sup> battery using the Cu<sub>95</sub>Co<sub>5</sub> aerogel cathode at 2 mA cm<sup>-2</sup>. (f-i) Photographs of Cu<sub>95</sub>Co<sub>5</sub> aerogel-based Zn-NO<sub>3</sub><sup>-</sup> battery powering electronic timer.

discharges normally at current densities ranging from 1 mA cm<sup>-2</sup> to 50 mA cm<sup>-2</sup>, demonstrating good rate performance (relevant information for Cu and Co can be found in Supporting Information, Fig. S36). At low to medium current densities (1–10 mA cm<sup>-2</sup>), the battery maintains a high potential (1.35–1.45 V), while at higher current densities (50 mA cm<sup>-2</sup>), the potential drops to around 1.10 V, indicating significant polarization. After high-rate discharge, the battery recovers to around 1.40 V, showing good dynamic recovery performance. These results indicate that, despite significant polarization at high current densities, the Zn-NO<sub>3</sub><sup>-</sup> battery overall exhibits a high open-circuit voltage, good electrochemical stability, and strong current output capability, providing solid performance support for practical applications. The stability of the Zn-NO<sub>3</sub><sup>-</sup> battery based on Cu<sub>95</sub>Co<sub>5</sub> was further evaluated through constant current charge-discharge cycling experiments. As shown in Fig. 6e, at a current density of 2 mA cm<sup>-2</sup>, the battery remains stable after 50 charge-discharge cycles without significant performance degradation. Additional cycling data (Fig. S37)

revealed that the battery could operate continuously for 36 hours without short-circuiting (Fig. S37a), sustain repeated cycling over extended periods (Fig. S37b), and achieve a peak round-trip energy efficiency of 60% in the first 37 hours (~110 cycles), which remained above 50% before declining likely due to nitrate depletion in the electrolyte (Fig. S37c). The system exhibited nearly 100% Coulombic efficiency over 140 cycles (Fig. S37d) and maintained a constant areal capacity of 0.334 mAh·cm<sup>-2</sup> (Fig. S37e), indicating exceptional cycling stability. Compared to other reported NO<sub>3</sub>RR-based systems (Table S7), the Zn-NO<sub>3</sub><sup>-</sup> battery with Cu<sub>95</sub>Co<sub>5</sub> cathode demonstrates competitive round-trip efficiency, near-ideal Coulombic efficiency, and stable capacity retention. Although gradual efficiency decay was observed over prolonged cycling—attributed to nitrate consumption—the system retained strong electrochemical reversibility and consistent discharge capacity, underscoring its promise as an energy storage technology coupled with nitrate reduction. Furthermore, as shown in Figs. 6f–i, the Zn-NO<sub>3</sub><sup>-</sup> battery based on Cu<sub>95</sub>Co<sub>5</sub> is capable of





providing continuous power for over 12 hours to a typical electronic timer, indicating stable current output and demonstrating its potential as a power source in practical applications.

## Conclusions

This study demonstrates that Co-doped Cu aerogels ( $\text{Cu}_{95}\text{Co}_5$ ) synthesized via a one-step co-reduction method achieve exceptional electrocatalytic nitrate-to-ammonia conversion, with 94.91% Faradaic efficiency and  $31.15 \text{ mg mg}_{\text{cat}}^{-1} \text{ cm}^{-2} \text{ h}^{-1}$   $\text{NH}_3$  yield at  $-0.7 \text{ V}$  vs. RHE. The combination of operando spectroscopy (SERS, ATR-FTIR, DEMS) and density functional theory (DFT) calculations elucidate a stepwise hydrogenation pathway:  $^*\text{NO}_3 \rightarrow ^*\text{NO}_2 \rightarrow ^*\text{NO} \rightarrow ^*\text{NH}_2\text{OH} \rightarrow ^*\text{NH}_3$ , with the rate-determining step (RDS) identified as  $^*\text{NO}$  hydrogenation to  $^*\text{NHO}$  and identified Co doping's pivotal roles: (1) Inducing lattice strain (11.22% Cu contraction) to optimize optimizes the d-band center, and tunes the adsorption energies of reactants and intermediates at active sites; (2) The incorporation of Co induces an upshift in the d-band center, thereby optimizing the adsorption-desorption kinetics of critical nitrogenous intermediates and promoting superior catalytic performance. (3) Enhancing interfacial  $\text{K}^+\text{H}_2\text{O}$  interactions to accelerate water dissociation and  $^*\text{H}$  generation; (4) Elevating the  $\text{NO}_2 \rightarrow \text{NH}_3$  rate constant ( $k_2$ : 48.93% higher than pure Cu) through electronic synergy. The hierarchical porosity of the aerogel facilitated mass transport while suppressing HER. Practical viability was confirmed via a  $\text{Zn-NO}_3^-$  battery delivering stable power for >12 h. These findings establish Cu-Co aerogels as a model system for sustainable  $\text{NH}_3$  synthesis, emphasizing metastable phase engineering and interfacial water modulation as critical design principles for next-generation  $\text{NO}_3\text{RR}$  catalysts.

## Author contributions

Ming Mu: Conceptualization, Experiments, Formal analysis, Software, Writing - original draft. Junjie Chen: Conceptualization, Investigation. Xiangxin Xue: Investigation. Yumei Yang: Investigation, Formal analysis. Ruikai Qi: Investigation. Yuezhu Wang: Investigation. Di Liu: Formal analysis. Lijia Shang: Formal analysis. Wenji Jiang: Investigation. Xinyi Shao: Investigation. Zheng-jie Chen: DFT calculations. Bing Zhao: Resources. Wei Song: Supervision, Conceptualization, Resources, Writing - review & editing.

## Conflicts of interest

There are no conflicts to declare.

## Data availability

Data will be made available on request.

## Acknowledgements

This work was supported by the research grants from the National Natural Science Foundation of China (22474048, 22074051).

## References

- H. Zhang, H. Wang, X. Cao, M. Chen, Y. Liu, Y. Zhou, M. Huang, L. Xia, Y. Wang and T. Li, *Adv. Mater.* 2024, **36**, 2312746.
- H. Zhang, K. Fang, J. Yang, H. Chen, J. Ning, H. Wang and Y. Hu, *Coordin. Chem. Rev.* 2024, **506**, 215723.
- J. Liang, Z. Li, L. Zhang, X. He, Y. Luo, D. Zheng, Y. Wang, T. Li, H. Yan and B. Ying, *Chem.* 2023, **9**, 1768-1827.
- D.-C. Zhong, Y.-N. Gong, C. Zhang and T.-B. Lu, *Chem. Soc. Rev.* 2023, **52**, 3170-3214.
- S. Han, H. Li, T. Li, F. Chen, R. Yang, Y. Yu and B. Zhang, *Nat. Catal.* 2023, **6**, 402-414.
- S. Bhowmick, A. Adalder, A. Maiti, S. Kapse, R. Thapa, S. Mondal and U. K. Ghorai, *Chem. Sci.* 2025, **16**, 4806-4814.
- S. Sarkar, A. Adalder, S. Paul, S. Kapse, R. Thapa and U. K. Ghorai, *App. Catal. B: Environ.* 2024, **343**, 123580.
- N. Mukherjee, A. Adalder, N. Barman, R. Thapa, R. Urkude, B. Ghosh and U. K. Ghorai, *J. Mater. Chem. A* 2024, **12**, 3352-3361.
- A. Adalder, S. Paul, N. Barman, A. Bera, S. Sarkar, N. Mukherjee, R. Thapa and U. K. Ghorai, *Acs. Catal.* 2023, **13**, 13516-13527.
- A. Adalder, K. Mitra, N. Barman, R. Thapa, S. Bhowmick, U. K. Ghorai, *Adv. Energy Mater.* 2024, **14**, 2403295.
- U. K. Ghorai, S. Paul, B. Ghorai, A. Adalder, S. Kapse, R. Thapa, A. Nagendra and A. Gain, *Acs Nano* 2021, **15**, 5230-5239.
- J. Liu, Z. Li, C. Lv, X.-Y. Tan, C. Lee, X. J. Loh, M. H. Chua, Z. Li, H. Pan, J. Chen, *Mater. Today* 2024, **73**, 208-2597.
- Z. Yu, M. Gu, Y. Wang, H. Li, Y. Chen and L. Wei, *Adv. Energy Sust. Res.* 2024, **5**, 2300284.
- Y. Wang, S. Wang, Y. Fu, J. Sang, P. Wei, R. Li, D. Gao, G. Wang and X. Bao, *Nat. Commun.* 2025, **16**, 897.
- W. Hiramatsu, Y. Shiraishi, S. Ichikawa, S. Tanaka, Y. Kawada, C. Hiraiwa and T. Hirai, *J. Am. Chem. Soc.* 2024, **147**, 1968-1979.
- J. Chen, M. Li, X. Wang, H. Liu, W. Jiang, B. Zhao and W. Song, *Angew. Chem. Int. Ed.* 2025, **64**, e202424986.
- D. Liu, P. Duan, J. Chen, M. Mu, Y. Yang, F. Ma, B. Zhao and W. Song, *Laser Photonics Res.* 2025, e01214.
- J. Yu, Y. Liu, C. Fan, N. Liu, J. Yin, Y. Li, Y. Cheng, X. Yuan, X. Zhang, Y. Liu, S. Fan, L. Xu and H. Li, *Nano Res.* 2025, **18**, e94907135.
- Y. Cui, C. Sun, G. Ding, M. Zhao, X. Ge, W. Zhang, Y. Zhu, Z. Wang and Q. Jiang, *Sci. China Mater.* 2023, **66**, 4387-4395.
- W. Yang, Z. Chang, X. Yu, P. Wu, R. Shen, L. Wang, X. Cui, and J. Shi, *Adv. Sci.* 2025, **12**, 2416386.
- W. He, J. Zhang, S. Dieckhöfer, S. Varhade, A.C. Brix, A. Lielpetere, S. Seisel, J. R. Junqueira and W. Schuhmann, *Nat. Commun.* 2022, **13**, 1129.
- S.-N. Zhang, P. Gao, Q.-Y. Liu, Z. Zhang, B.-L. Leng, J.-S. Chen and X.-H. Li, *Nat. Commun.* 2024, **15**, 10877.
- J. Chen, X. Xing, S. Wen, M. Li, W. Jiang, X. Shao, R. Qi, Y. Yang, M. Mu, Z. Chen, B. Zhao and W. Song, *Chem. Eng. J.* 2025, **521**, 167002.
- H. Wang, J. Huang, J. Cai, Y. Wei, A. Cao, B. Liu and S. Lu, *Small Methods* 2023, **7**, 2300169.
- B. Wang, K. Li, G. Xu, Z. Zhang, X. Wang, J. Sun, Y. Song, X. Zhang, Y. Liang, D. Kong, Y. Qiu, Q. Teng, X. Cui, J. Chen, J. Zhao, J. Wang,



## ARTICLE

## Journal Name

- H. Yang, J. Huang and Y. Tang, *Angew. Chem. Int. Ed.* 2025, **64**, e202502725.
26. S. J. Hwang, S.-K. Kim, J.-G. Lee, S.-C. Lee, J. H. Jang, P. Kim, T.-H. Lim, Y.-E. Sung and S. J. Yoo, *J. Am. Chem. Soc.* 2012, **134**, 19508-19511.
27. X. Wu, F. Chen, N. Zhang, Y. Lei, Y. Jin, A. Qaseem and R. L. Johnston, *Small* 2017, **13**, 1603387.
28. L. Qiao, A. Zhu, D. Liu, K. An, J. Feng, C. Liu, K. W. Ng and H. Pan, *Adv. Energy Mater.* 2024, **14**, 124528
29. H.-Q. Chen, H. Ze, M.-F. Yue, D.-Y. Wei, Y.-L. A, Y.-F. Wu, J.-C. Dong, Y.-J. Zhang, H. Zhang, Z.-Q. Tian and J.-F. Li, *Angew. Chem. Int. Ed.* 2022, **134**, e202117834.
30. T. Zhang, J. Lv, R. Yang, Z. Yan, X. Sun, X. Xu and Y. Liu, *Adv. Energy Mater.* 2024, **14**, 2400790.
31. W. Zheng, L. Zhu, Z. Yan, Z. Lin, Z. Lei, Y. Zhang, H. Xu, Z. Dang, C. Wei and C. Feng, *Environ. Sci. Technol.* 2021, **55**, 13231-13243.
32. J. Yu, R.-T. Gao, X. Guo, N. T. Nguyen, L. Wu and L. J. Wang, *Angew. Chem. Int. Ed.* 2025, **64**, e202415975.
33. S. J. Zheng, X. Y. Dong, H. Chen, R. W. Huang, J. Cai and S. Zang, *Angew. Chem. Int. Ed.* 2025, **64**, e202413033.
34. J. Ni, J. Yan, F. Li, H. Qi, Q. Xu, C. Su, L. Sun, H. Sun, J. Ding and B. Liu, *Adv. Energy Mater.* 2024, **14**, 2400065.
35. Y. Li, Z. Lu, L. Zheng, X. Yan, J. Xie, Z. Yu, S. Zhang, F. Jiang and H. Chen, *Energy Environ. Sci.* 2024, **17**, 4582-4593.
36. W. Gao, K. Xie, J. Xie, X. Wang, H. Zhang, S. Chen, H. Wang, Z. Li and C. Li, *Adv. Mater.* 2023, **35**, 2202952.

View Article Online  
DOI: 10.1039/D5SC04633E



**Data availability statements**

View Article Online  
DOI: 10.1039/D5SC04633E

The data supporting this article have been included as part of the Supplementary Information.

